Chem. Res. Chin. Univ., 2016, 32(6), 902—911 doi: 10.1007/s40242-016-6056-z

Synthesis, Structural Study and Phase Transitions Characterization by Thermal Analysis and Vibrational Spectroscopy of an Ammonium Rubidium Arsenate Tellurate

GHORBEL Khouloud[1*], LITAIEM Hajer[1], KTARI Lilia[1], GARCIA-GRANDA Santiago[2] and DAMMAK Mohamed[1]

1. Laboratoire de Chimie Inorganique(LCI), Université de Sfax, Faculté des Sciences de Sfax, BP 1171 Sfax 3000, Tunisia;
2. Laboratoire de Chimie Physique et Analytique, Faculté de Chimie, Université d'Oviedo, Oviedo 33006, Espagne

Abstract The $Rb_{2.42}(NH_4)_{0.58}(HAsO_4)(H_2AsO_4)\cdot Te(OH)_6$ crystals(denoted by RbNAsTe) crystallize in the monoclinic system, space group $P2_1/n$ with the following parameters: a=1.3059(5) nm, b=0.6755(3) nm, c=1.6675(6) nm, β=94.126(4)°, Z=4 and V=1.46733(10) nm^3. Thermal analyses(DSC, DTA and TG) confirm the presence of the phase transition and the temperature of the decomposition. The vibrational spectroscopy study at room temperature show the presence and the independence of anionic groups, cationic groups, and give more importance to the hydrogen bonds. Raman spectra were recorded in the temperature range of 298—503 K. The temperature dependence of the Raman line shift, intensity reduction and the half width detects the phase transitions and confirms their nature. So, the phase transition at 453 K corresponds to the superprotonic-ionic conduction phase transition, and those at 483 and 491 K correspond to the decomposition of our material.

Keywords RbNAsTe; X-Ray diffraction; Differential scanning calorimetry; Phase transition; Raman spectrometry

1 Introduction

Inorganic materials with hydrogen bonds are well known for their high-temperature phase transition with high proton mobility showing superprotonic conduction[1,2]. They are also known for their low temperature phases showing ferroelectricity[3,4]. These materials are used in many fields of applications such as multilayer capacitors, microelectronic components, material of storage of energy. Much interest has been focused on the compounds of general formula $M_2XO_4\cdot Te(OH)_6$(M= Na^+, K^+, NH_4^+, Rb^+ ⋯ and X=S[5,6], Se[7,8], P[9—11], As[12,13]) and $(NH_4)_{2x}M_{2-2x}SO_4\cdot Te(OH)_6$(M=Rb, Na, K, Cs)[14—16]. These families open perspectives to examine a structure type with different cationic groups' combinations thanks to their structural and physical properties. Ammonium rubidium sulfate tellurate, $Rb_{1.12}(NH_4)_{0.88}(SO_4)\cdot Te(OH)_6$(RbNSTe), and rubidium arsenate tellurate, $Rb_2HAsO_4\cdot Te(OH)_6$(RbAsTe), which are centrosymmetric, crystallize in the monoclinic system $P2_1/a$ and $P2_1/c$, respectively[17,18]. To the best of our knowledge, the studies of the crystal structure and dielectric properties pertaining to the partial cationic substitution(Rb^+ by NH_4^+) have not been undertaken especially in the family of $M_2HAsO_4\cdot Te(OH)_6$[13,17]. The effects of the partial anionic substitution on crystal symmetry and physical properties have been investigated in previous research works for the mixed solution of ammonium arsenate sulfate tellurate $(NH_4)_2(SO_4)_{0.92}H(AsO_4)_{0.08}\cdot Te(OH)_6$[19]. In the aim of studying the influence of cationic substitution on the chemical and structural characteristics, the present study investigates and discusses the results of a structural study pertaining to a new solution $Rb_{2.42}(NH_4)_{0.58}(HAsO_4)(H_2AsO_4)\cdot Te(OH)_6$. This structural study is accompanied with thermal analyses [differential scanning calorimetry(DSC), thermodifference analysis(DTA), differential thermogravimetric analysis(TG)] and vibrational spectroscopy.

2 Experimental

2.1 Chemical Preparation

Colorless and transparent crystals of the title compound were produced from an aqueous solution containing a stoichiometric mixture of telluric acid H_6TeO_6, arsenic acid H_3AsO_4, ammonium carbonate $(NH_4)_2CO_3$ and rubidium carbonate Rb_2CO_3, with the following reaction:

$$3/2x(NH_4)_2CO_3 + 3/2(1-x)\,Rb_2CO_3 + 2H_3AsO_4 + H_6TeO_6 \longrightarrow (NH_4)_{3x}Rb_{3-3x}(HAsO_4)(H_2AsO_4)\cdot Te(OH)_6 + 3/2CO_2 + 3/2H_2O \quad (1)$$

The resulting solution was kept under ambient conditions and evaporated slowly. The aqueous solution was filtered with a micro-filter after three recrystallizations and a good single crystal was obtained. The $Rb_{2.42}(NH_4)_{0.58}(HAsO_4)(H_2AsO_4)\cdot$

*Corresponding author. E-mail: ghorbelkhouloud@yahoo.fr

Received February 17, 2016; accepted March 22, 2016.

Supported by the Ministry of Higher Education and Research of Tunisia and Spanich(No.MINECOMAT2013-40950-R) and the European Regional Development Fund.

$Te(OH)_6$(denoted by RbNAsTe) compound was noted to be stable in air and its formula was determined by the chemical analysis and confirmed by the refinement of the crystal structure.

2.2 Single-crystal X-ray Diffraction

The unit cell dimensions were refined using the indexation of diffractometer reflections collected with Agilent Xcalibur Gemini RCCD diffractometer, with graphite monochromatized Mo $K\alpha$(λ=0.0710 nm). The data were processed with Oxford Diffraction Crys Alis CCD and Crys Alis RED[20]. Software and Empirical absorption correction using spherical harmonics were implemented with SCALE3 ABSPACK scaling algorithm. The crystal structure was solved and refined against F^2. All calculations were performed using the SHELX86 computer programs included in the Crystals software package[21]. We solved the structure firstly by locating the Te, Rb and As atoms by Patterson methods and subsequently by the deduction of the O, N and H atom positions from the difference Fourier maps. When all atoms were anisotropically refined, the agreement factors R and wR converged to 0.063 and 0.065, respectively. The details of data collection and refinement of the title compound are summarized in Table 1. The final positions and equivalent isotropic thermal parameters of the RbNAsTe compound are given in Tables S1 and S2(see the Electronic Supplementary Material of this paper).

The structure graphics were created by the Diamond program[22].

Table 1 Main crystallographic, feature X-ray diffraction data, parameters and results of RbNAsTe*

Chemical formula	$Rb_{2.42}(NH_4)_{0.58}(HAsO_4)(H_2AsO_4)\cdot Te(OH)_6$
Color/shape	Colourless/parallelepiped
Temperature/K	293
Crystal system	Monoclinic
Space group	$P2_1/n$
a/nm	1.3059(5)
b/nm	0.6755(3)
c/nm	1.6675(6)
β/(°)	94.126(4)
V/nm^3	1.46733(10)
Z	4
F(000)	1339.828
Formula weight/(g·mol^{-1})	727.88
μ/mm^{-1}	14.55
ρ_{cal}/(g·cm^{-3})	3.295
Min/max Brag angle/(°)	3.3/31.5
Index ranges	$-18\leqslant h\leqslant 18$, $-9\leqslant k\leqslant 9$, $-23\leqslant l\leqslant 24$
Parameters refined	150
Reflections with $I>2\sigma(I)$	1589
Independent reflexions	4437
Mesured reflections	14332
GOOF	0.9603
R_{int}	0.036
$R_1[F^2>4\sigma(F)^2]$	0.063
$wR_2(F^2)$	0.065

* R values are defined as $wR_2=\{\sum[w(F_0^2-F_c^2)^2]/w(F_0^2)^2\}^{1/2}$ and $R_1=\sum||F_0|-|F_c||/\sum|F_0|$.

2.3 Thermal Analysis

The differential scanning calorimetry(DSC) measurements were carried out by means of a Mettler Toledo DSC model DSC822 with samples placed inside platinum crucibles at a heating rate of 10 K/min. Besides, the simultaneous TG and DTA analyses were performed with Mettler Toledo model TGA851ELF and Setaram model Setsys Evolution 16 thermobalances. The samples, whose masses in TG and DTA measurements were 25.83 mg, were placed inside uncovered alumina crucibles. They were heated from 298 K to 1200 K at a heating rate of 10 K/min. In the TG test, a Pfeiffer Vacuum ThermoStar^{TM} GSD301 T mass spectrometer was used to determine the evacuated vapors.

2.4 Vibrational Spectroscopy Measurements

The infrared absorption spectra of the crystalline suspension in KBr were recorded using a Jasco-FT-IR-420 spectrophotometer in the 400—4000 cm^{-1} frequency range. The Raman spectra of polycrystalline samples sealed in glass tubes were recorded on a micro-Raman spectrometer(Horiba HR 800, Jobin Yvon), working on a back scattering configuration, equipped with a He-Ne laser(λ=632 nm). The spectral resolution of the system is 3 cm^{-1}.

3 Results and Discussion

3.1 Structural Properties

The $Rb_{2.42}(NH_4)_{0.58}(HAsO_4)(H_2AsO_4)\cdot Te(OH)_6$ crystallized in the monoclinic space group $P2_1/n$ at room temperature, with the unit cell parameters: a=1.3059(5) nm, b=0.6755(3) nm, c=1.6675(6) nm, β=94.126(4)°, Z=4 and V=1.46733(10) nm^3. However, the RbAsTe crystallized in the monoclinic space group $P2_1/c$ with the unit cell parameters: a=0.8344(2) nm, b=0.712(10) nm, c=1.2453(2) nm, β=90.28(1)°, Z=4 and V=0.74001(2) nm^3[17]. The unit cell parameters increase, *i.e.*, the cell volume of RbNAsTe double that of the RbAsTe, which may be due to the size of the partial substitution. When the RbNSTe structure crystallized in the monoclinic space group $P2_1/a$ with different unit cell parameters, a=1.1438(5) nm, b=0.6643(3) nm, c=1.3700(4) nm, β=106.896(2)°, Z=4 and V=0.9960(8) nm^3[18], the cell volume of RbNAsTe is superior to that of RbNSTe, which may be due to the difference between the anions bulk. A projection of the crystal structure of RbNAsTe on the bc plane is depicted in Fig.1. From this projection, the structure can be described to be built of planes of pure AsO_4 tetrahedra and pure TeO_6 octahedra alternating with Rb^+/NH_4^+ cations that are statistically disordered over the same site. Actually, two AsO_4 tetrahedra layers and one TeO_6 octahedra layer are observed. The Rb^+/NH_4^+ cations are intercalated between these polyhedra. The stability of the crystal structure is assured by the linkage of different polyhedra with two types of hydrogen bonds O—H···O and N—H···O and through the electrostatic actions of the NH_4^+ and Rb^+ cations. It can be seen in Fig.S1(see the Electronic Supplementary

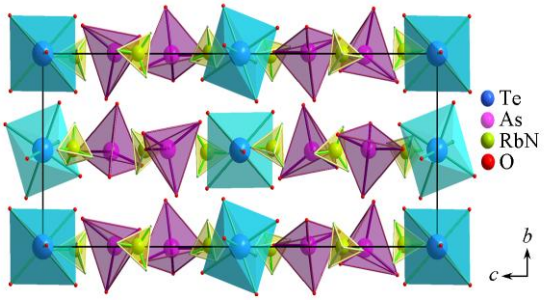

Fig.1 Projection of crystal structure of RbNAsTe in the *bc* plane

Material of this paper) that the TeO_6 occupies an octahedral site formed by AsO_4 and Rb/NH_4 polyhedra. The room temperature crystal structure of RbNAsTe was found to be similar to that of RbAsTe. It is the atomic arrangement and the degree of distortion of the corresponding AsO_4 tetrahedra and TeO_6 octahedra that make the analogy between these structures important. The overall structure of the three compounds can be described as a sequence of planes of mixed polyhedra: TeO_6 octahedra and AsO_4 tetrahedra, parallel to the *ab* plane, and the cations assure the cohesion between them, although RbAsTe and RbNSTe compounds are not isostructural with RbNAsTe. The presence of two types of TeO_6 octahedra differing in their distortion is noted in the structure of RbNAsTe. In fact, the Te atoms occupy two special positions with 0.5 occupancy runs. While in the first phase, the site symmetries correspond to an inversion center, in the second one, they correspond to the binary axis site.

The main interatomic distances and bond angles are reported in Table 2. As can be seen, the TeO_6 coordination octahedra are not very symmetrical. The Te—O distances in $Te1O_6$ octahedra range from 0.1896(18) nm to 0.1938(9) nm and angles O—Te1—O are between 87.40(4)° and 92.60(4)°, whereas in $Te2O_6$ octahedra, the Te—O distances vary from 0.1888(12) nm to 0.1900(11) nm, and the O—Te2—O angles range from 87.10(7)° to 92.90(7)°, indicating that the shape of $Te1O_6$ is slightly distorted from that of $Te2O_6$, but both are distorted. The values of Te—O distances are noted to be very close to those observed in the original compound. In the RbAsTe material, the Te atom occupies only one general position. The Te—O distances spread from 0.1905(13) nm to 0.1913(14) nm and O—Te—O angles range from 87.67(7)° to 92.33(7)°. Contrary to the rubidium arsenate tellurate, the RbNAsTe structure presents two types of AsO_4 tetrahedra in general positions with 1.000 occupancy runs(Fig.2). In the first tetrahedra $As1O_4$, the length of the As—O bonds vary between 0.1664(13) nm and 0.1710(9) nm and O—As—O angles vary from 104.4(10)° to 112.8(7)°, whereas in $As2O_4$ tetrahedra, the As—O distances are between 0.1668(8) nm and 0.1734(14) nm, and O—As—O angles range from 103.40(9)° to 113.70(5)°. Then, Δd(As—O) and $\Delta\angle$(O—As—O) are 0.0046 nm and 8.4° in As1 and 0.0066 nm and 10.3° in As2. So, the shape of $As1O_4$ tetrahedra is more regular than that of $As2O_4$, which can be caused by the presence of hydrogen bonds that play an important role in the As—O length. In the structures of the present study and previous research works on compounds containing the arsenate

Table 2 Selected bond distances(nm) and angles(°) in the RbNAsTe material*

Te1—O1#1	0.1934(19)	As1—O10	0.1664(13)	N2/Rb2—O12#9	0.3000(12)
Te1—O3#1	0.1938(9)	As2—O11	0.1668(8)	N2/Rb2—O14#10	0.3008(14)
Te1—O2#1	0.1896(18)	As2—O12	0.1678(11)	N2/Rb2—O6#11	0.3023(16)
Te1—O1	0.1934(19)	As2—O13	0.1734(14)	N2/Rb2—O13#12	0.3057(13)
Te1—O2	0.1896(18)	As2—O14	0.1678(12)	N2/Rb2—O6#9	0.3101(18)
Te1—O3	0.1938(9)	N1/Rb1—O5#3	0.2891(13)	N2/Rb2—O4#11	0.3112(14)
Te2—O4#2	0.1900(11)	N1/Rb1—O7	0.2911(9)	N2/Rb2—O10#12	0.3292(15)
Te2—O5#2	0.1888(12)	N1/Rb1—O12#4	0.2992(13)	N3/Rb3—O1#14	0.2822(10)
Te2—O6#2	0.1888(15)	N1/Rb1—O1	0.3002(19)	N3/Rb3—O10#14	0.2893(14)
Te2—O4	0.1900(11)	N1/Rb1—O2	0.3003(19)	N3/Rb3—O1	0.2930(20)
Te2—O5	0.1888(12)	N1/Rb1—O13#1	0.3027(14)	N3/Rb3—O8	0.2947(14)
Te2—O6	0.1888(12)	N1/Rb1—O9#5	0.3063(15)	N3/Rb3—O2#14	0.3020(20)
As1—O7	0.1710(9)	N1/Rb1—O8#6	0.3246(14)	N3/Rb3—O4#15	0.3163(13)
As1—O8	0.1677(13)	N1/Rb1—O14#7	0.3425(12)	N3/Rb3—O7#5	0.3301(12)
As1—O9	0.1686(13)	N2/Rb2—O3#8	0.2822(10)	N1/Rb1—O9#5	0.3358(14)
O1#1—Te1—O3#1	91.8(9)	O4#2—Te2—O5#2	90.9(5)	O7—As1—O8	104.4(10)
O1#1—Te1—O2#1	87.4(4)	O4#2—Te2—O6#2	89.2(7)	O7—As1—O9	105.7(6)
O3#1—Te1—O2#1	90.1(9)	O5#2—Te2—O6#2	92.9(7)	O8—As1—O9	110.2(7)
O3#1—Te1—O1	88.2(9)	O5#2—Te2—O4	89.1(5)	O7—As1—O10	111.5(8)
O2#1—Te1—O1	92.6(4)	O6#2—Te2—O4	90.8(7)	O8—As1—O10	112.8(7)
O1#1—Te1—O2	92.6(4)	O4#2—Te2—O5	89.1(5)	O9—As1—O10	111.8(7)
O3#1—Te1—O2	89.9(9)	O6#2—Te2—O5	87.1(7)	O11—As2—O12	113.7(5)
O1#1—Te1—O2	87.4(4)	O4—Te2—O5	90.9(5)	O11—As2—O13	103.4(9)
O1#1—Te1—O3	88.2(9)	O4#2—Te2—O6	90.8(7)	O12—As2—O13	107.2(6)
O2#1—Te1—O3	89.9(9)	O5#2—Te2—O6	87.1(7)	O11—As2—O14	113.1(7)
O1—Te1—O3	91.8(9)	O4—Te2—O6	89.2(7)	O12—As2—O14	109.9(6)
O2—Te1—O3	90.1(9)	O5—Te2—O6	92.9(7)	O13—As2—O14	109.2(7)

* Symmetry codes: #1: $-x, -y, -z$; #2: $-x, -y, -z-1$; #3: $x, y, z+1$; #4: $-x, -y-1, -z$; #5: $-x+1/2, y+1/2, -z+1/2$; #6: $-x+1/2, y-1/2, -z+1/2$; #7: $x-1/2, -y-1/2, z+1/2$; #8: $x+1, y, z$; #9: $x+1/2, -y-1/2, z+1/2$; #10: $-x+1, -y-1, -z$; #11: $-x+1/2, y+1/2, -z-1/2$; #12: $-x+1, -y, -z$; #13: $-x+1/2, y-1/2, -z-1/2$; #14: $x, y+1, z$; #15: $x+1/2, -y+1/2, z+1/2$; #16: $x-1/2, -y-1/2, z-1/2$; #17: $x-1/2, -y+1/2, z-1/2$; #18: $x, y-1, z$.

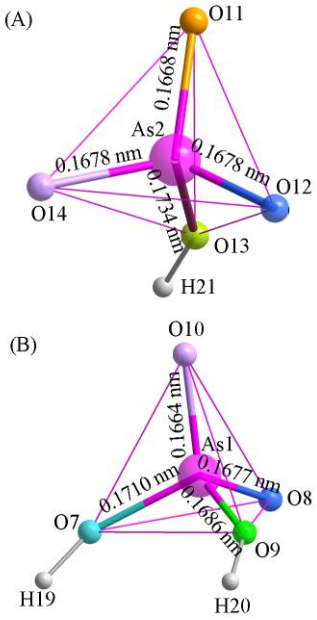

Fig.2 Projection of AsO_4 tetrahedra in RbNAsTe compound

group, it is possible to use differences in bond lengths to identify with which O the proton is more highly associated[23—25]. Referring to Table 2, we note that among the eight As—O bonds lengths in the two tetrahedra $As1O_4$ and $As2O_4$, there are three As—O bonds that are significantly longer than the others. The longest As—O bonds concern oxygen atoms O7, O9 and O13, which are covalently bonded to H19, H20 and H21. Whereas, the other As—O bonds concern oxygen atoms O8, O10, O11, O12 and O14, which are not associated with any proton. Consequently, two oxygen atoms belonging to $As1O_4$ tetrahedra are linked to two hydrogen atoms to form $H_2AsO_4^-$ and one oxygen atom belonging to $As2O_4$ tetrahedra is connected to a hydrogen atom to form $HAsO_4^{2-}$ ions.

As shown in Fig.3, the arrangement of the different polyhedra in the new mixed compound RbNAsTe forms Tunnels, as in the RbAsTe material. Unlike the tunnels of the latter, which are square cross section, those of RbNAsTe are parallelogram cross section where Rb/N cations are placed. The sides of the parallelogram are equal to 0.6758 and 0.735 nm. In contrast with RbNSTe and RbAsTe, The Rb/N atoms are distributed over three sites. Indeed, Rb1/N1 is coordinated by nine oxygen atoms with Rb1/N1—O distances spread from 0.2891(13) nm to 0.3425(12) nm. Both Rb2/N2 and Rb3/N3 are coordinated by eight oxygen atoms, with Rb2/N2—O distances between 0.2926(9) nm and 0.3292(15) nm and Rb3/N3—O distances varying from 0.2822(10) nm to 0.3358(14) nm. In the first site, Rb/N is coordinated by three oxygen atoms belonging to $As1O_4$ tetrahedra, three belonging to $As2O_4$ tetrahedra, two belonging to $Te1O_6$ octahedra and only one belonging to $Te2O_6$ octahedra. In the second site, it is coordinated by one oxygen atom belonging to $Te1O_6$ octahedra, three belonging to $Te2O_6$ octahedra, three belonging to $As2O_4$ tetrahedra and only one belonging $As1O_4$ tetrahedra. In the third site, Rb/N is coordinated by four oxygen atoms belonging to $As1O_4$ tetrahedra, two belonging to $Te1O_6$ octahedra and only one belonging to $Te2O_6$ octahedra. The rubidium/ammonium coordination atom is shown in Fig.S2(see the Electronic Supplementary Material of this paper) and Table 2.

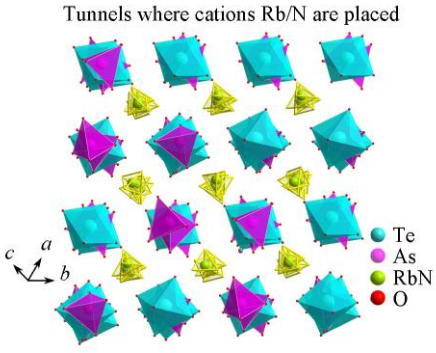

Fig.3 Representation of tunnels in the RbNAsTe structure

Fig.4 depicts a projection view of the title compound, indicating the hydrogen bonding in RbNAsTe. The geometrical characterizations of the hydrogen bonds network are listed in Table 3. The stability of the crystal structure of RbNAsTe is guaranteed by two types of hydrogen bonds. On the one hand, the O—H···O hydrogen bond assured the connection between the arsenate tetrahedra and the tellurate octahedra. On the other hand, the N—H···O assured the connection between anionic groups and ammonium groups. According to the Brown theory, the cohesion of the structure is assured by strong and weak hydrogen bonds. The O···O distances are between 0.2555(8) nm and 0.3374(3) nm, the O···H distances vary from 0.1783(4) nm to 0.2530(2) nm and the O—H···O angles are between 127.10(8)° and 172.80(1)°. These values are slightly higher than those found in RbAsTe structure. Thus, the insertion of NH_4^+ with Rb^+ in RbAsTe can be deduced to decrease the stability of this structure. Together with the O—H···O hydrogen bonding, the structure of this mixed compound is stabilized by N—H···O hydrogen bonding. All of the hydrogen atoms belonging to the first, the second and the third type of NH_4^+ group contribute in the formation of this kind of hydrogen bond except for H8. The obtained O—H distances vary from 0.1961 nm to 0.2558 nm and N—H···O angles are between 121.90(8)° and 159.70(3)°. The presence of the two types of hydrogen bonds is in the origin of the protonic conduction phase transition at high temperature.

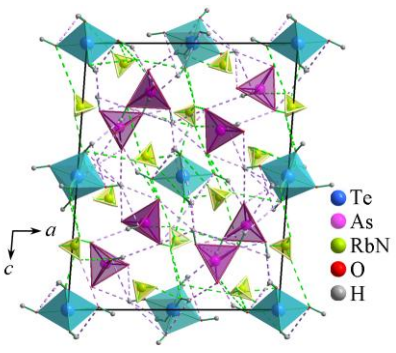

Fig.4 Projection of the RbNAsTe structure showing the hydrogen bonds

Table 3 Hydrogen bonds in the RbNAsTe compound*

D—H···A	$d_{D—H}$/nm	$d_{H\cdots A}$/nm	$d_{D—A}$/nm	∠D—H···A/(°)
O3—H3···O10#1	0.0967(2)	0.2029(3)	0.2822(2)	137.9(13)
O4—H4···O11#16	0.0948(2)	0.2521(5)	0.3374(3)	149.9(8)
O5—H5···O9 #11	0.0958(4)	0.2395(5)	0.3262(9)	150.4(8)
O5—H5···O10# 11	0.0958(4)	0.2020(4)	0.2708(4)	127.1(8)
O7—H19···O8#6	0.0959(5)	0.1783(4)	0.2555(8)	135.2(16)
O9—H20···O1#6	0.0959(4)	0.2304(1)	0.3257(11)	172.8(10)
O13—H21···O12#11	0.0940(2)	0.2530(2)	0.3370(2)	149.0(9)
O1—H1···N3	0.0935(4)	0.2192(4)	0.2933(2)	135.55(13)
O2—H2···N3#18	0.0972(3)	0.2202(8)	0.3018(3)	140.7(12)
O4—H4···N3#17	0.0948(5)	0.2394(3)	0.3164(1)	138.2(8)
O6—H6··· N2#16	0.0981(3)	0.2391(9)	0.3102(4)	128.9(10)
O13—H21···N2#12	0.0940(4)	0.2453(7)	0.3056(4)	121.9(8)
N1—H7···O12#4	0.0950(3)	0.2247(3)	0.2993(4)	134.8(3)
N1—H9···O2	0.0950(3)	0.2309(3)	0.3001(3)	129.2(5)
N1—H10···O7	0.0950(4)	0.1961(3)	0.2911(9)	180.0(7)
N2—H11···O10#12	0.0950(4)	0.2387(4)	0.3294(8)	159.7(3)
N2—H12···O14#10	0.0950(2)	0.2116(5)	0.3007(7)	155.7(3)
N2—H13···O4#11	0.0950(5)	0.2473(8)	0.3111(5)	124.4(3)
N2—H13···O13#12	0.0950(2)	0.2324(3)	0.3056(3)	133.5(4)
N3—H15···O11#14	0.0950(2)	0.2063(4)	0.2823(2)	135.9(3)
N3—H16···O4#15	0.0950(4)	0.2437(4)	0.3164(1)	133.2(3)
N3—H16..O10#14	0.0950(3)	0.2143(3)	0.2894(7)	135.0(4)
N3—H17···O9#5	0.0950(3)	0.2558(3)	0.3358(4)	142.0(3)
N3—H18···O8	0.0950(2)	0.2239(1)	0.2944(5)	130.3(4)

* Symmetry codes: #1: $-x, -y, -z$; #2: $-x, -y, -z-1$; #3: $x, y, z+1$; #4: $-x, -y-1, -z$; #5: $-x+1/2, y+1/2, -z+1/2$; #6: $-x+1/2, y-1/2, -z+1/2$; #7: $x-1/2, -y-1/2, z+1/2$; #8: $x+1, y, z$; #9: $x+1/2, -y-1/2, z+1/2$; #10: $-x+1, -y-1, -z$; #11: $-x+1/2, y+1/2, -z-1/2$; #12: $-x+1, -y, -z$; #13: $-x+1/2, y-1/2, -z-1/2$; #14: $x, y+1, z$; #15: $x+1/2, -y+1/2, z+1/2$; #16: $x-1/2, -y-1/2, z-1/2$; #17: $x-1/2, -y+1/2, z-1/2$; #18: $x, y-1, z$.

3.2 Thermal Analysis

The DSC measurements were taken by heating a sample from 320 K to 800 K. Fig.5 shows the temperatures of the phase transitions estimated from the peak positions. Three endothermic peaks appear at T_1=453 K, T_2=483 K and T_3=491 K. Since the second and third peaks are overlapping, the former hides the latter. From the DSC thermogram, it is shown that the enthalpy associated with the first transition is distinctly small compared with that associated with the second and the third transitions. Hence, the enthalpy and entropy of these phase transitions cannot be calculated separately. Consequently, the enthalpy and entropy for the sum of these peaks are ΔH= 426.3 J/g and ΔS=91.064×10^{-2} J·g^{-1}·K^{-1}. Fig.6 presents the TG, DTG and DTA curves, which show no mass loss between room temperature and 475 K. Indeed, the first peak observed in DSC at T_1=453 K can be attributed to a super-ionic-protonic

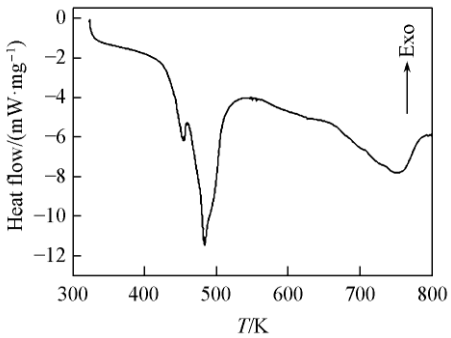

Fig.5 DSC curve of RbNAsTe material

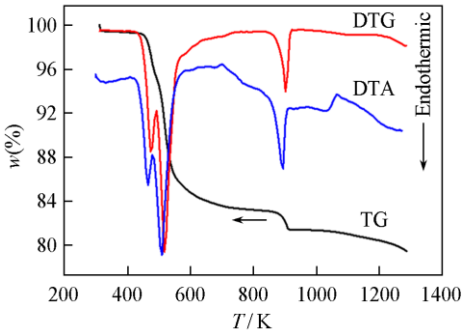

Fig.6 TG-DTG-DTA curves of RbNAsTe material

conduction phase transition, whereas the intense peak at T_2=483 K accompanied with a shoulder at T_3=491 K is probably attributed to a decomposition[26]. The conducted Raman spectroscopy investigations confirm the presence and nature of these phase transitions detected by DSC.

TG-DTG curves demonstrate the total mass loss of 18% from room temperature up to 1000 K. The mass loss can be described by three separate and defined steps. The stage in the range between approximately 472 K and 492 K(reaching its maximum velocity at 475 K), associated with a small endothermic peak on the DTA curve, corresponds to the loss of water molecules. Actually, in the temperature range of 400—500 K, the telluric acid $Te(OH)_6$ decomposes to disengage the water molecule and give the orthotelluric acid H_2TeO_4[27]. The decomposition of the new material can be described by the following reaction:

$$Rb_{2.42}(NH_4)_{0.58}H(AsO_4)H_2(AsO_4)\cdot Te(OH)_6 \longrightarrow Rb_{2.42}(NH_4)_{0.58}H(AsO_4)H_2(AsO_4)\cdot H_2TeO_4 + 2H_2O \quad (2)$$

The second step, between 492 K and 720 K approximately (reaching its maximum velocity at 520 K), associated with an endothermic peak on the DTA at 512 K, corresponds to the loss of three water molecules and ammonia molecule[mass loss 12%(calcd. 11.06%)]. Moreover, in the temperature range of 523—673 K, orthotelluric acid H_2TeO_4 begins to decompose with the water liberation and oxygen beginning to escape at 578 K[27]. This phenomenon is shown in the decomposition of telluric acid $Te(OH)_6$ and some additional compounds, such as $(NH_4)_2(SO_4)_{0.92}H(AsO_4)_{0.08}\cdot Te(OH)_6$[19]. Furthermore, the hydrogen-arsenate $HAsO_4$ acid decomposes to disengage the water and oxygen molecule and gives the As_2O_3[28].

The rest of the mass loss between 720 K and 920 K approximately(reaching its maximum velocity at 900 K)[mass loss 2%(calcd. 1.99%)], associated with an endothermic peak on the DTA at 890 K, corresponds to the loss of O_2 molecule.

3.3 Vibrational Spectroscopy Study

3.3.1 Vibrational Spectroscopy Study at Room Temperature

In order to confirm the presence and independence of ions groups(TeO_6^{6-}, AsO_4^{3-}, Rb^+ and NH_4^+) and to identify the hydrogen bonds in RbNAsTe, the Infrared and Raman spectra of this new compound were investigated in the range of 400—4000 cm^{-1} and 50—4000 cm^{-1}, respectively, and shown in Fig.7 and Fig.8. The proposed assignments of the different bands(Table 4) were carried out using data for similar arsenate tellurate compounds. The obtained IR and Raman bands of RbNAsTe can be divided into three frequency regions: the bands below 250 cm^{-1} are due to the external modes which contain the translations of Rb^+ and lattice mode[6,29]; the frequency range of 250—1000 cm^{-1} can be attributed to the internal modes of AsO_4 and TeO_6[29—37]; the frequency range of 1200—3700 cm^{-1} can be accredited to the internal vibrations of NH_4^+ and high-frequency hydrogen modes[14,29].

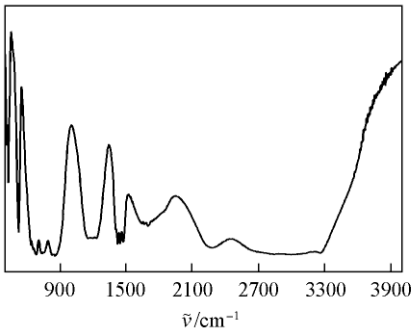

Fig.7 IR spectrum of RbNAsTe compound at room temperature

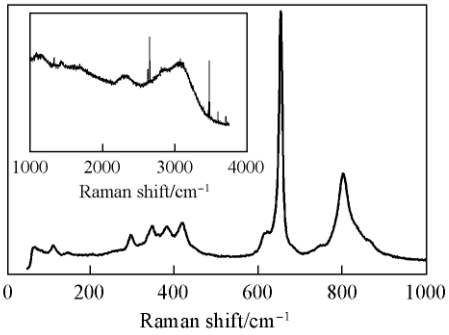

Fig.8 Raman spectra of RbNAsTe compound at room temperature

The strong Raman band noticed at 746 cm^{-1}, which is expected to be a shoulder at 743 cm^{-1} in the infrared spectra, can be attributed to $\nu_1(AsO_4)$[30,31]. While, the medium band observed in the Raman spectra at 296 cm^{-1} can be assigned to the $\nu_2(AsO_4)$ bending vibration. $\nu_3(AsO_4)$ is distinguished by the very intense and broad Raman band at about 801 cm^{-1} and by the broad infrared band at 836 cm^{-1}[32]. The $\nu_4(AsO_4)$ group is detected by a Raman band at 418 cm^{-1} and by three infrared bands at 411, 418 and 428 cm^{-1}, which is in accordance with group theory[17]. The very weak lines between 145 cm^{-1} and 200 cm^{-1} in Raman spectra can be attributed to the motion of O—H···O hydrogen stretching($\nu_{O\cdots O}$) and bending($\nu_{O\cdots O}$) of the $H_2AsO_4^-$ and $HAsO_4^{2-}$[38].

The most intense peaks around 653 cm^{-1} in Raman and 681 cm^{-1} in IR are assigned to $\nu_1(TeO_6)$[6,29,33]. The shoulder and broad peaks at 617 and 629 cm^{-1} in Raman and IR spectra, respectively, are attributed to $\nu_2(TeO_6)$. Moreover, the peaks detected at 411 cm^{-1} in IR and 382 cm^{-1} in Raman correspond to $\nu_5(TeO_6)$. The $\nu_6(TeO_6)$ and $\nu_4(TeO_6)$ vibration modes appear only in Raman spectra at 346 and 296 cm^{-1}[29,34,35]. The bands linked to the vibration modes of NH_4^+ ions are more visible at frequencies upper to 1300 cm^{-1}. The large massive IR band at 3253 cm^{-1} and Raman band at 3073 cm^{-1} correspond to $\nu_3(NH_4^+)$. Nevertheless, the very weak IR band observed at 1402 cm^{-1}, which appears at 1433 cm^{-1} in Raman, is assigned to $\nu_4(NH_4^+)$. The $\nu_2(NH_4)$ mode appears at 1697 cm^{-1} in IR spectra and 1677 cm^{-1} in Raman spectra[14,29]. The strong and broad band near 1140—1230 cm^{-1} in IR can be assigned to the δ(As—O—H) bending vibration[17,32,36]. The very shoulder peaks at 1421, 1443 and 1473 cm^{-1} in IR spectra can be attributed to the hydrogen bending modes $\delta(OH)$[32,33]. Other information that can be obtained from the vibrational spectra pertains to the strength and type of O—H···O hydrogen bonds. The stretching vibration related to the strong hydrogen bonds gives rise to the characteristic broad triobands of ABC type[39—42]. The very broad lines at 2845, 2327 and 1677 cm^{-1} in Raman spectra can be assigned to the ABC bonds of OH stretching vibrations in RbNAsTe, respectively. The vibrational studies at room temperature confirm the coexistence of the TeO_6^{6-}, AsO_4^{3-}, Rb^+ and NH_4^+ independently, which provides evidence to our last structural description.

3.3.2 Vibrational Spectroscopy Study at High Temperature

To get more information about the phase transition mechanisms in RbNAsTe, the temperature evolution of the Raman bands has been performed in the frequency region between 50 cm^{-1} and 1200 cm^{-1} and in the temperature range from 298 K to 503 K to validate the probable changes in the spectra around the 453 K phase transition. The vibrational analyses of

Table 4 Infrared and Raman data for RbNAsTe*

IR, $\tilde{\nu}$/cm^{-1} (T=298 K)	Raman shift/cm^{-1} T=298 K	T=303 K	T=383 K	Assignment
3253vw	3073w	—	—	$\nu_3(NH_4)$ and ν_{OH} of $Te(OH)_6$
—	2845vw	—	—	ν(OH) of strong hydrogen bond
2281w	2327vw	—	—	
1697w	1677w	—	—	$\nu_2(NH_4)$
1473sh	—	—	—	δ(OH)
1443sh	1433vw	—	—	
1421sh	—	—	—	
1402sh	—	—	—	$\nu_4(NH_4)$
1230w	—	—	—	δ(As–O–H)
1140w	1159w	—	—	
863sb	850wbr	862	859	
835br	—	836	834	
—	801vs	804	806	$\nu_3(AsO_4)$
743s	746s	748	744	$\nu_1(AsO_4)$
681sb	684wbr	680	682	
—	653vs	654	652	$\nu_1(TeO_6)$
637s	629sh	644	642	
—	612sh	617	618	$\nu_2(TeO_6)$
522vs	—	—	—	
428s	418m	419	416	$\nu_4(AsO_4)$
418w	—	—	—	
411w	382m	383	383	$\nu_5(TeO_6)$
—	346m	345	347	$\nu_6(TeO_6)$
—	296m	297	296	$\nu_4(TeO_6)$ and $\nu_2(AsO_4)$
	258sh	259	—	$T(NH_4^+)$
	—	201	201	ν(OH···O)
	147br	150	146	δ(OH···O)
	114br	113	108	Lattice modes
	67br	67	67	$T(Rb^+)$

Raman shift/cm^{-1} T=403 K	T=423 K	T=443 K	T=463 K	T=483 K	T=503 K	Assignment
854	852	874	881	881	885	
831	831	827	—	826	—	
809	810	800	808	797	807	$\nu_3(AsO_4)$
724	722	725	725	720	728	$\nu_1(AsO_4)$
680	679	681	679	682	677	
652	654	653	653	657	657	$\nu_1(TeO_6)$
639	640	635	—	—	—	$\nu_2(TeO_6)$
628	629	525	525	539	535	
418	400	409	411	391	401	$\nu_4(AsO_4)$
385	381	369	362	360	366	$\nu_5(TeO_6)$
360	364	358	—	336	340	$\nu_6(TeO_6)$
—	—	—	305	302	306	
261	289	271	270	272	272	$\nu_4(TeO_6)$ and $\nu_2(AsO_4)$
—	247	257	244	231	231	
202	202	201	192	200	200	ν(OH···O)
146	148	146	146	146	—	Lattice modes
108	104	—	—	—	—	
72	69	67	68	71	70	$T(Rb^+)$

* Relative intensities: vs: very strong; s: strong; m: medium; sh: shoulder; vw: very weak; w: weak; br: broad; wbr: weak broad.

the broad temperature range have also been conducted to obtain further information about the role of anion contributions to the mechanism of the phase transition in RbNAsTe compounds. For this reason, a detailed analysis of position, intensity reduction and full width at half height(FWHM) of the bands has been carried out at temperatures below and above the phase transition temperature. Since the wavenumber region corresponds to the bands emanating from the vibration modes of the anionic units, the changes are likely to be associated with the different dynamical state of both ions below and above the phase transition point.

From the thermal Raman spectra evolution of the mixed compound presented in Fig.9, it can be deduced that there are significant changes in the position, intensity and FWHM of the bands corresponding to the internal vibrations when temperature increases from room temperature to 503 K. Therefore, the

phase transition at 450 K has been proven in this compound by Raman spectroscopy. The position, intensity and FWHM of the Raman lines were refined using a combination of Gaussian and Lorentzian functions. Fig.10 shows an example of the deconvolution of the Raman spectrum while Fig.11 and Fig.12 reveal the temperature dependence of the wavenumbers, the intensity and the FWHM of the vibration modes of TeO_6^{6-} and AsO_4^{3-}. The dashed vertical lines mark the transition and the estimated decomposition temperatures. When the temperature increases

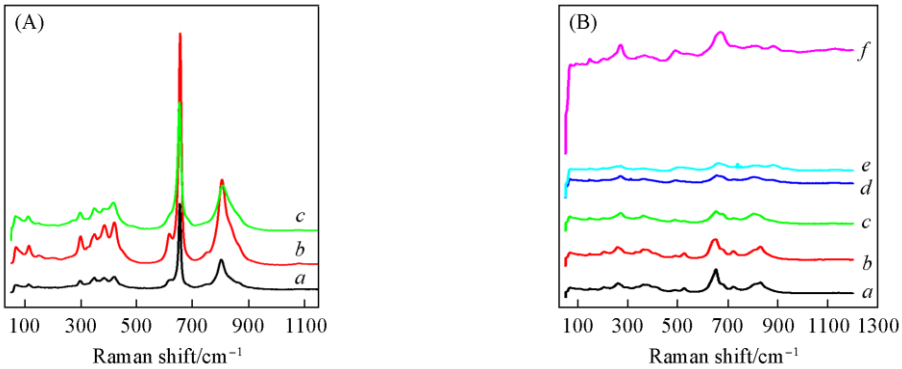

Fig.9 Raman spectra of RbNAsTe compound at various temperatures

T/K: (A) *a*. 298, *b*. 305, *c*. 383; (B) *a*. 403, *b*. 423, *c*. 443, *d*. 463, *e*. 483, *f*. 503.

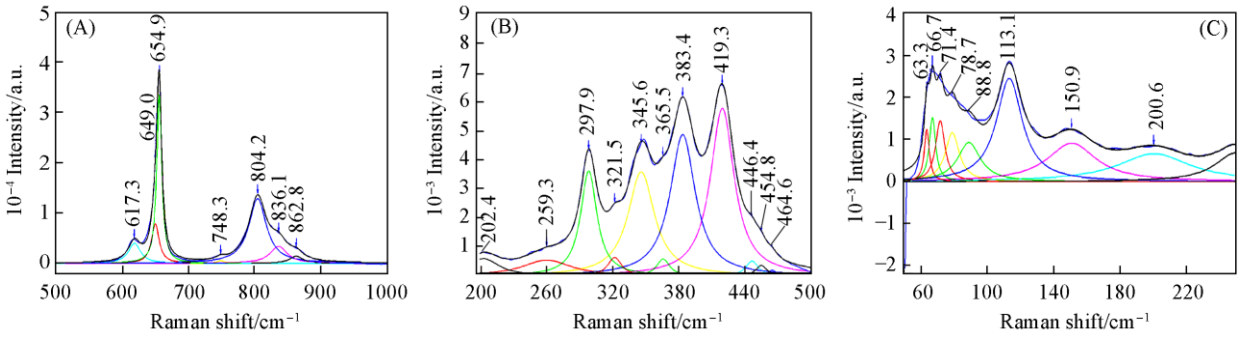

Fig.10 Deconvolution of the Raman spectra of RbNAsTe compound at *T*= 303 K

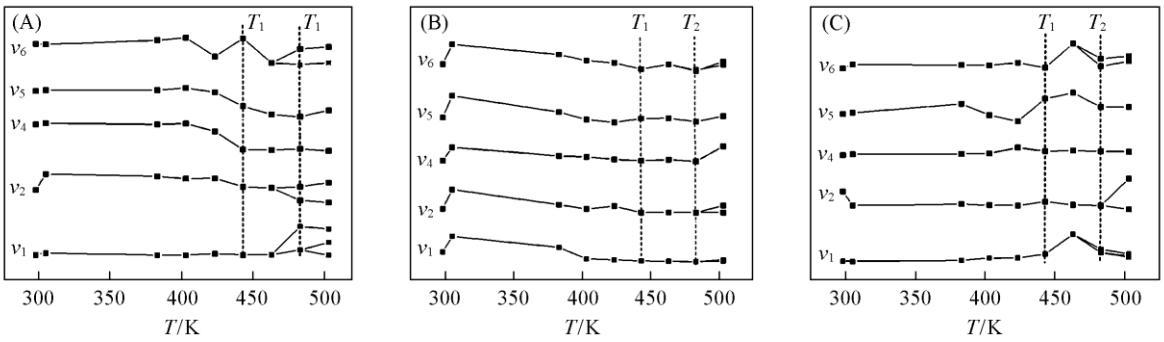

Fig.11 Temperature dependence of wavenumber(A), intensity(B) and FWHM(C) of the vibration modes of TeO_6 in RbNAsTe compound

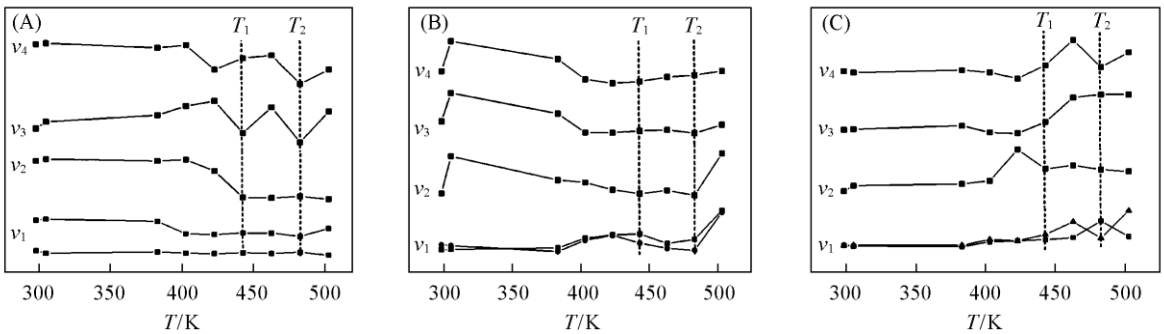

Fig.12 Temperature dependence of wavenumber(A), intensity(B) and FWHM(C) of the vibration modes of AsO_4 in RbNAsTe compound

from room temperature to 463 K, the major bands of the vibration modes of TeO_6^{6-} shift to low frequencies[Fig.11(A)]. In the temperature range of 298—423 K, the position shift of the bands corresponding to $v_2(TeO_6)$, $v_4(TeO_6)$ and $v_5(TeO_6)$ conserves its linear character and becomes discontinuous at T=443 K. The position shift of these bands ranges from about –8, –18 and –12 cm^{-1} for $v_2(TeO_6)$, $v_4(TeO_6)$ and $v_5(TeO_6)$, respectively. The temperature of discontinuity is supposed to be the temperature of the phase transition, which is in accordance with the DSC result. Above 443 K, the position shift of $v_2(TeO_6)$ and $v_4(TeO_6)$ recovers its linearity when the temperature increases. Likewise, $v_6(TeO_6)$ shows significant transformation on the wavenumber shift when the temperature comes close to the phase transition temperature at 443 K. All the analyzed bands of the vibration modes of TeO_6^{6-} on heating from 298 K to 483 K increase in intensity at 303 K followed by a continuous rating decrease[Fig.11(B)]. This behavior may be due to a disorder of anionic groups. The temperature effect can also be seen in the temperature dependence of FWHM[Fig.11(C)]. So, the Raman bands broaden with the increase in temperature in the common temperature dependence. It is known that the significant increase of the line width could be due to the anharmonicity and disordering bands of TeO_6^{6-} ions. But, an additional anomaly such as a jump change of the bandwidth can be due to the presence of a phase transition. Indeed, since all the vibration modes of TeO_6^{6-} are affected, $v_1(TeO_6)$, $v_4(TeO_6)$, $v_5(TeO_6)$, $v_6(TeO_6)$ show an important variation at 463 K, although the latter is shown at 443 K for $v_2(TeO_6)$[Fig.11(C)]. In the 298—463 K interval, Fig.12(A) shows a major variation of the position of $v_3(AsO_4)$ and $v_4(AsO_4)$ at 463 K. As for $v_2(AsO_4)$ position in function of temperature, it conserves its linear character in the temperature range of 298—423 K, hence proving the lack of changes in the geometry of AsO_4 bands in the ring. Similarly, in the case of the vibration mode of TeO_6, $v_2(AsO_4)$ loses its linearity at 423 K and becomes discontinuous at T= 443 K. At this temperature, the wavenumber shift of this band ranges from about –18 cm^{-1}, which can be interpreted as the phase transition. Above 443 K, the band of stretching vibration of AsO_4 shifts linearly with the increase in temperature. Fig.12(B) shows the temperature dependence of the vibration modes of AsO_4^{3-}. As in the above case, the vibration modes of this group mark an increase in intensity at 303 K followed by a continuous decrease up to 483 K. Fig.12(C) shows a significant transformation of the half-widths of the bands associated with the internal vibrations of AsO_4^{3-}, especially when the temperature draws near the temperature of phase transition. Thus, we come to the conclusion that both TeO_6^{6-} and AsO_4^{3-} groups contribute in the phase transition at 453 K. But TeO_6^{6-} seems to be the more sensitive one to the spectrum changes. These results are in accordance with the previous study[26]. Actually, the phase transition observed in the thermal analysis can be accredited to a super ionic-protonic conduction[26]. Therefore, this compound is characterized by a large proton conduction due to the presence of two types of hydrogen bonds O—H···O and N—H···O. It is also characterized by the influence of the addition of protons to the anionic groups $As1O_4^{3-}$ and $As2O_4^{3-}$. That is why the arsenic group participates in this super-protonic conduction. So, the presence of proton guarantees the high conduction near the decomposition temperature. These phenomena of super- protonic conduction at high temperature especially before the decomposition can be explained by the breaking of hydrogen bonds.

Moreover, we have undertaken a Raman spectrum at a temperature up to 463 K for three reasons. The first one is to shed the light on the presence of the phase transitions observed in DSC at 483 and 491 K. The second one is to confirm that these phase transitions are attributed to the decomposition of this material. As for the last one, it is to demonstrate that the process of the anionic groups plays a key role. The wavenumber of telluric group as a function of temperature shows significant changes, on heating to 483 K. In fact, the $v_2(TeO_6)$ band observed at 629 cm^{-1} splits into two bands at 632 and 619 cm^{-1}. Whereas, the line observed at 653 cm^{-1} corresponding to $v_1(TeO_6)$ reveals an important change of position with the movement to higher frequencies at 483 K and shift up to 4 cm^{-1}, then at 503 K, it splits into two lines at 652 and 665 cm^{-1}. This phenomenon is observed in the vibration mode $v_6(TeO_6)$. Actually, the peak at 346 cm^{-1} seems to merge in an important and very broad double peak at 483 K. The vibration mode of AsO_4 tetrahedra shows an important fluctuation at 503 K, and the temperature evolution of $v_1(AsO_4)$ is seen in the spectrum as a shift by –7 cm^{-1} at 483 K. So, the line found at 752 cm^{-1} disappears at 503 K, which leads to the conclusion that telluric acid is responsible for the decomposition at T= 483 and 491 K. These results accord well with those obtained previously by the thermal analysis, indicating that the progressive decomposition of telluric acid in the temperature between 472 K and 492 K is due to the disengagement of two water molecules, giving the orthotelluric acid TeO_4^{4-} [27]. In fact, in the Raman spectra of RbNAsTe at 503 K, the triply degenerate mode $v_4(TeO_4)$ appears at 306, 340 and 366 cm^{-1}, whereas $v_2(TeO_4)$ appears at 491 cm^{-1}. The appearance of a new peak at 882 cm^{-1} is assigned to $v_1(TeO_4)$. While, the vibration $v_3(TeO_4)$ appears to be around 636, 652 and 665 cm^{-1}[13,43,44]. The vibration mode of AsO_4 tetrahedra is still active at T= 503 K, the vibration of $v_1(AsO_4)$ appears around 680 and 728 cm^{-1}, that of $v_3(AsO_4)$ appears around 808 cm^{-1}. The bands at 270 and 401 cm^{-1} are assigned to $v_2(AsO_4)$ and $v_4(AsO_4)$, respectively.

4 Conclusions

The new mixed compound $Rb_{2.42}(NH_4)_{0.58}(HAsO_4)\cdot(H_2AsO_4)\cdot Te(OH)_6$ crystallized in monoclinic space group $P2_1/n$. X-ray studies showed that the title compound has an interesting three dimensional network. Besides, the structure is made up of planes of mixed octahedra and tetrahedra, with the NH_4^+ and Rb^+ cations intercalating between them. In addition to the electrostatic actions of the cations, the material cohesion of this compound is assured by O—H···O hydrogen bonds

between anion/anion and N—H···O hydrogen bonds between anion/ cation. Three phase transitions at T_1=453 K, T_2=483 K and T_3=491 K have been evidenced by DSC and DTA analyses. The TG curve shows that no mass loss was detected between room temperature up to 475 K. The temperature evolution of Raman spectra reveals the existence of phase transitions and confirms their nature. The transitions at T_1=453 K would be a super- protonic conduction, whereas the transitions at T_2=483 K and T_3=491 K would rather be related to the decomposition. According to the Raman results, the super-protonic conduction can be seen as related to TeO_6^{6-} and AsO_4^{3-} groups, which can be explained by the breaking of hydrogen bonds. The telluric acid is responsible for the decomposition of our material, which decomposes into a orthotelluric acid.

Acknowledgments

The authors would like to express their thanks to Dr. Khemakhem H. for his help in the spectroscopic Raman measurements.

Supplementary Material

Further details of the Inorganic Crystal Structure(ICSD) can be obtained from FIZ Karlsruhe-Leibniz Institute for Information Infrastructure Hermann-von-Helmholtz-Platz 1-76344 Eggenstein-Leopoldshafen; Fax: +(49)7247808-666; Tel: +(49)7247808-337; E-mail: dorothea.ariman@friz-karlsruhe.ac.de(or at www.fiz-karlsruhe.de/kontakt.html) on quoting the deposit number ICSD: 429446.

Electronic Supplementary Material

Supplementary material is available in the online version of this article at http://dx.doi.org/10.1007/s40242-016-6056-z.

References

[1] Litaiem H., Dammak M., Mhiri T., Cousson A., *Alloys Compd.*, **2005**, *396*, 34

[2] Dammak M., Khemakhem H., Mhiri T., *Phys. Chem. Solids*, **2001**, *62*, 2069

[3] Ktari L., Dammak M., Hadrich A., Cousson A., Nierlich M., Romain F., Mhiri T., *Solid State Sci.*, **2004**, *6*, 1393

[4] Ktari L., Dammak M., Madani A., Mhiri T., *Solid State Ionics*, **2001**, *145*, 225

[5] Zilber R., Durif A., Averbuch-Pouchot M. T., *Acta Cryst.*, **1981**, *B37*, 650

[6] Dammak M., Khemekhem H., Mhiri T., Kolsi A. W., Daoud A., *Alloys Compd.*, **1998**, *280*, 107

[7] Dammak M., Litaiem H., Gravereau P., Mhiri T., Kolsi A. W., *Alloys Compd.*, **2007**, *442*, 316

[8] Dammak M., Khemakhem H., Zouari N., Kolsi A. W., Mhiri T., *Solid State Ionics*, **2000,** *127*, 125

[9] Averbuch-Pouchot M. T., *Acta Cryst.*, **1992**, *48*, 973

[10] Boudjada N., Boudjada A., Guitel J. C., *Acta Cryst.*, **1983**, *39*, 656

[11] Durif A., Averbuch-Pouchot M. T., Guitel J. C., *Acta Cryst.*, **1979**, *35*, 1444

[12] Bechibani I., Litaiem H., Ktari L., Garcia-Granda S., Dammak M., *Mol. Struct.*, **2014**, *1075*, 579

[13] Bechibani I., Litaiem H., Ktari L., Zouari N., Garcia-Granda S., Dammak M., *Phys. Chem. Solids*, **2014**, *75*, 911

[14] Ktari L., Dammak M., Kolsi A. W., Cousson A., *Alloys Compd.*, **2009**, *476*, 54

[15] Dammak M., Ktari L., Cousson A., Mhiri T., *Solid State Chem.*, **2005**, *178*, 2109

[16] Ktari L., Dammak M., Mhiri T., Savariault J. M., *Solid State Chem.*, **2000**, *16*, 1

[17] Bechibani I., Litaiem H., Ktari L., Lhoste J., Dammak M., *Mol. Struct.*, **2013**, *1045*, 199

[18] Ktari L., Dammak M., Mhiri T., Kolsi A. W., *Phys. Chem. News*, **2002**, *8*, 1

[19] Ghorbel K., Litaiem H., Ktari L., Garcia-granda S., Dammak M., *Mol. Struct.*, **2015**, *1079*, 225

[20] *CrysAlis CCD and CrysAlis RED*, Oxford Diffraction Ltd., Yarnton, Oxfordshire, **2010**

[21] Betteridge P. W., Carruthers J. R., Cooper R. I., Watkin K., *Appl. Cryst*., **2003**, *36*, 1487

[22] Brandenburg K., Berndt M., *Diamond. Version 2.1.b*, Crystal Impact Gb R, Bonn, **1999**

[23] Ferraris G., Jones D. W., Yerkess J., *Acta Crystallogr*, **1972**, *B28*, 2430

[24] Ferraris G., Angela M. F., *Acta Crystallogr*, **1973**, *B29*, 286

[25] Naïli H., Vendier L., Jaud J., Mhiri T., *Solid State Sci*., **2001**, *3*, 677

[26] Ghorbel K., Litaiem H., Ktari L., Garcia-Granda S., Dammak M., *Ionics,* **2016**, *22*, 251

[27] Faby J., Loub J., Feltl L., *Therm. Anal*., **1982**, *24*, 95

[28] Ekambaram S., Sevov S. C., *Inorg. Chem*., **2000**, *39*, 2405

[29] Litaiem H., Dammak M., Ktari L., Kammoun S., Mhiri T., *Phase Transitions*, **2004**, *77*, 929

[30] Jrifi A., El Jazouli A., Chaminade J. P., Couzi M., *Powder Diffr.*, **2009**, *24*(3), 200

[31] Dhouib I., Elaoud Z., Mhiri T., Daoud A., *J. Chem. Crystallogr.*, **2012**, *42*, 513

[32] Amri M., Zouari N., Mhiri T., Gravereau P., *Alloys Compd*., **2009**, *477*, 68

[33] Jarraya K. H., Gublin N., Guermani N., Mhiri T., *Mater. Sci. Eng.,* **2012**, *28*, 012046

[34] Chabchoub N., Khemakhem H., Von der mühll R., *Alloys Compd*., **2005**, *386*, 319

[35] Dammak M., Hadrich A., Mhiri T., *Alloys Compd*., **2007**, *428*, 8

[36] Bortun A. I., Bortun L. N., Clear Field A., Trobajo C., Garcia J. R., *Mater. Res. Bull.*, **1998**, *33*(4), 583

[37] Hadrich A., Lautie A., Mhiri T., *Raman Spectrosc*., **2000**, *31*, 587

[38] Lecalve N., Romain F., Limage M. H., Novak A., *Mol. Struct.*, **1989**, *200*, 131

[39] Marchon B., Novak A., *Chem. Phys*., **1985**, *78*, 2105

[40] Ohno N., Lockwood D. J., *Chem. Phys*., **1985**, *83*, 4374

[41] Choi B. K., Kim J. J., *Appl. Phys*., **1985**, *24*, 914

[42] Baran J., *Mol. Struct*., **1987**, *162*, 211

[43] Siebert H., Anorg Z., Allgen V., *Chem*., **1959**, *301*, 161

[44] Farmer V. C., *Mineralogical Society Monograph 4: the Infrared Spectra of Minerals*, the Mineralogical Society, London, **1974**